JPhys Energy

PAPER • OPEN ACCESS

Exploring battery cathode materials in the Li-Ni-O phase diagrams using structure prediction

To cite this article: Jiayi Cen *et al* 2023 *J. Phys. Energy* **5** 035005

IOP Publishing J. Phys. Energy 5 (2023) 035005 https://doi.org/10.1088/2515-7655/acdd9c

Journal of Physics: Energy

OPEN ACCESS

RECEIVED
10 February 2023

REVISED
26 May 2023

ACCEPTED FOR PUBLICATION
12 June 2023

PUBLISHED
28 June 2023

PAPER

Exploring battery cathode materials in the Li-Ni-O phase diagrams using structure prediction

Jiayi Cen[1,2], **Bonan Zhu**[1,2] **and David O Scanlon**[1,2,*]

[1] Department of Chemistry and Thomas Young Centre, University College London, 20 Gordon Street, London WC1H 0AJ, United Kingdom
[2] The Faraday Institution, Quad One, Harwell Science and Innovation Campus, Didcot OX11 0RA, United Kingdom
[*] Author to whom any correspondence should be addressed.

E-mail: d.scanlon@ucl.ac.uk

Keywords: lithium-ion batteries, *ab initio* random structure searching, density functional theory

Supplementary material for this article is available online

Abstract

The Li-Ni-O phase diagram contains several electrochemically active ternary phases. Many compositions and structures in this phase space can easily be altered by (electro-)chemical processes, yielding many more (meta-)stable structures with interesting properties. In this study, we use *ab initio* random structure searching (AIRSS) to accelerate materials discovery of the Li-Ni-O phase space. We demonstrate that AIRSS can efficiently explore structures (e.g. $LiNiO_2$) displaying dynamic Jahn-Teller effects. A thermodynamically stable $Li_2Ni_2O_3$ phase which reduces the thermodynamic stability window of $LiNiO_2$ was discovered. AIRSS also encountered many dynamically stable structures close to the convex hull. Therefore, we confirm the presence of metastable Li-Ni-O phases by revealing their structures and properties. This work will allow Li-Ni-O phases to be more easily identified in future experiments and help to combat the challenges in synthesizing Li-Ni-O phases.

Abbreviations

AIRSS	*ab initio* random structure searching
DFT	density functional theory
LIBs	Lithium-ion batteries
PES	potential energy surface
NFORM	number of formula units in the unit cell

1. Introduction

Lithium-ion batteries (LIBs) are popular energy storage technologies to power portable electronics. While there exist several working principles for LIBs, the principle based on the intercalation chemistry is better understood and many intercalation LIBs have been commercialized [1, 2]. The cathode components in those intercalation LIBs greatly dictate the energy densities and possess the largest occupancy of the raw materials cost (∼22%) [3, 4]. To promote a wide-scale adoption of LIBs in other sectors (e.g. transportation) requires developing cathode materials with lower cost and higher energy densities.

The earliest studied oxide cathode is the layered $LiCoO_2$ [3]. With the rising prices of cobalt and the geopolitical issues with its supply, nickel became a popular ingredient for cathodes since it is cheaper and more abundant [3, 5]. This led to the discoveries of ternary Li-Ni-O compounds such as $LiNiO_2$ and Li_2NiO_3 which eliminate the use of Co (see figure 1) [5–8]. The compositions and structures of several Li-Ni-O phases have very specific growth conditions. A subtle change in the Li/Ni ratio and oxygen partial pressure can lead to different structures [9]. This is because: (1) many of those structures are related as they are based on the same oxygen cubic close-packed (ccp) sublattice [9]; (2) Ni^{3+} and Ni^{4+} are difficult to stabilize and can be easily converted to Ni^{2+} (e.g. via disproportionations) [9–13]; (3) cation mixing becomes more

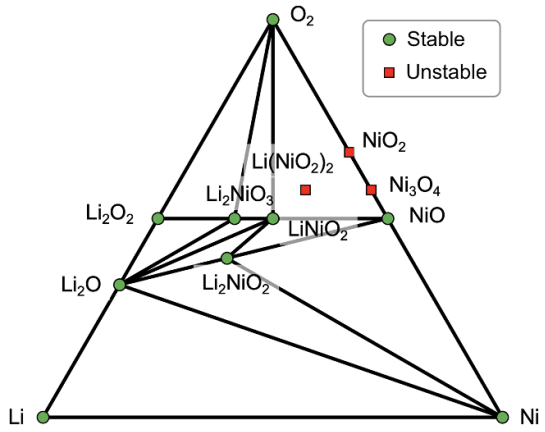

Figure 1. The Li-Ni-O phase diagram containing the commonly studied/reported ternary phases. The phase stability at 0 K was calculated using the PBEsol + U functional in VASP. The $LiNiO_2$, Li_2NiO_2 and Li_2NiO_3 are the experimentally known ternary phases.

favorable due to the similar ionic radii of Ni^{2+} (0.69 Å) and Li^+ (0.76 Å) and the magnetic frustration/interactions [5, 14, 15]. The superexchange interaction between neighboring Ni cations that are bridged by O anions is stronger in a (linear) interplane fashion between the antisite Ni^{2+} (upon Ni^{2+}/Li^+ exchange) and Ni cations in the transition metal (TM) layer, compared to the 90° intraplane superexchange between Ni in the TM layer. The interplane superexchange also relieves the magnetic frustration that arises from the intraplane interaction within the TM layer by providing different exchange paths [16]. Many more (meta)-stable structures could have been generated during (electro)-chemical processes. Some of them may exist in small quantities, which becomes difficult to isolate. However, there have been successful discoveries of new phases in this way. For example, the metastable $P\bar{3}m1$ Li_2NiO_2 (1T-Li_2NiO_2) was discovered by electrochemical Li insertion from $LiNiO_2$, charge compensated by Ni^{2+} [11, 17].

Another way to discover new structures is to use computational methods, where hundreds of structures can be evaluated in a shorter time and more cheaply compared to experiments[18]. AIRSS has become an increasingly popular method to access new structures [19–24]. It works by sampling the potential energy surface (PES) of various structural configurations in a random fashion. This method is highly parallel and there is a small number of easy-to-understand parameters to control the search efficiency. Chemical knowledge can be used to help the generation of sensible random structures, followed by geometry optimization using DFT calculations. This process is repeated until low energies structures are encountered multiple times. To reduce the computational cost of DFT calculations and structure search time, one can employ crystal symmetry to bias search towards lower local energy minima and/or selectively perform geometry optimizations with various convergence criteria [19].

In this work, we use AIRSS to explore structures in the Li-Ni-O phase diagram as we believe our chosen search space is enriched with many yet undiscovered (meta)-stable structures. To achieve this, we first re-explored the experimentally known Li-Ni-O systems to illustrate that AIRSS can effectively sample the PES and locate known structures. We then searched structures in 11 different hypothetical $Li_xNi_yO_z$ stoichiometries and investigated the lowest energy structures by evaluating their thermodynamic and dynamical stabilities (see table 1). Among many (meta-)stable phases we identified, the layered $Li_2Ni_2O_3$ and Li_4NiO_3 phases have comparable theoretical energy densities to $LiNiO_2$, and they share some structural features with 1T-Li_2NiO_2. The newly discovered thermodynamically stable $Li_2Ni_2O_3$ phase is a limiting phase which reduces the thermodynamic stability window of $LiNiO_2$.

2. Methods

Charge neutral $Li_xNi_yO_z$ compositions were enumerated by the SMACT code [25], assuming there are no mix-valent Ni ions. Compositions were restricted to have a total number of atoms in the empirical (reduced) formula $\leqslant$12 and the total number of atoms in the full formula $\leqslant$28. This gives a total of 14 compositions to be searched, of which three compositions ($LiNiO_2$, Li_2NiO_3 and Li_2NiO_2) have experimentally known structures. For the three experimentally known compositions, at least 2000 structures with number of formula units in the unit cell (controlled by the NFORM keyword) between 1 and 4 were generated and geometry optimized. For each of the 11 hypothetical compositions, around 500 structures (with NFORM $\leqslant$2) were generated and optimized. Search with NFORM = 4 was also performed on Li_3NiO_3 in search of

Table 1. The 11 hypothetical charge neutral compositions with no known experimental structures. Results were taken from the lowest energy structures with the ground state magnetic ordering optimized with PBEsol + U and HSE06 functionals (separately) in VASP. The $Li_2Ni_2O_5$ phase exceeds the threshold of energy above the Li-Ni-O convex hull (E_{above_hull}) of 100 meV atom^{-1}, hence no further calculations were performed.

#	Composition	Formal oxidation states on Ni	Composition reported on materials project database?	Thermodynamic stability (PBEsol + U) (meV atom^{-1})	Thermodynamic stability (HSE06) (meV atom^{-1})	Dynamically stable? (PBEsol + U)
1	$Li_2Ni_2O_3$	+2	No	0	0	Yes
2	Li_4NiO_3	+2	No	8.28	7.66	Yes
3	$Li_2Ni_4O_5$	+2	No	18.76	10.06	Yes
4	$Li_4Ni_2O_5$	+3	No	22.95	13.51	Yes
5	Li_3NiO_3	+3	Theoretical	31.28	17.62	Yes
6	$Li_2Ni_3O_4$	+2	No	31.91	22.28	Yes
7	Li_5NiO_4	+3	Theoretical	37.93	23.86	Yes
8	Li_4NiO_4	+4	No	43.52	30.33	Yes
9	Li_6NiO_4	+2	Theoretical	46.31	46.90	Yes
10	$LiNi_3O_5$	+3	No	65.55	103.17	Yes
11	$Li_2Ni_2O_5$	+4	No	145.33	—	—

lower energy structures. More information about the energy distribution of structures with respect to NFORM can be found on the "Additional information on the distribution of searched structures"section in the supplementary information document.

The open sourced AIRSS code was used to generate structures for each chosen composition [19, 20]. Sensible random structures were first generated with pre-assumed ferromagnetic (FM) spin states and then geometry optimized by the plane-wave DFT code CASTEP [26] (version 19.11). Spin-polarized calculations were performed using the PBEsol exchange-correlation XC functional [27] with Hubbard U correction ($U_{\text{eff}} = 6$ eV) for Ni d electrons (i.e. PBEsol + U) [28, 29]. The U value was taken from a previous study where it was fit to empirical oxidation energies [29, 30]. Results are expected to be insensitive to the exact values of U used, thus the same qualitatively trend should be observed unless a widely different U is used. Geometry optimizations were initially performed with a loose convergence setting (i.e. crude search). Monkhorst-Pack [31] meshes of k-points with a spacing of 0.07 2π Å^{-1} was used with plane-wave cutoff energy of 340 eV. The on-the-fly generated (OTFG) ultrasoft pseudopotentials QC5 were used [32, 33]. A subset of structures was then reoptimized using harder OTFG C19 pseudopotentials and with tighter convergence settings (700 eV energy cutoff and Monkhorst-Pack k-point spacing of 0.05 2π Å^{-1}) to refine the structures and their energetics (i.e. refined search).

Further structural optimization and property calculations were performed with the VASP code [34–36] on a selection of CASTEP optimized refined structures using the PBEsol + U ($U_{\text{Ni}} = 6$ eV) with a cutoff energy of 550 eV and a k-point spacing of 0.05 2π Å^{-1} on gamma-centered Monkhorst-Pack grids. A maximum force tolerance of 0.01 eV Å^{-1} was applied during geometry optimization. The PAW pseudopotentials [37, 38] (version PBE 5.4) of Li_*sv*, Ni_*pv* and O were used unless otherwise stated. Lattice dynamics calculations were performed on the known phases in the Li-Ni-O phase diagrams and the lowest energy structure in each hypothetical composition with the ground magnetic ordering using the Phonopy package [39] with the finite-displacement method at an increased cutoff energy of 800 eV and a tighter force tolerance of 0.001 eV Å^{-1} during geometry optimization (table S1). Non-analytical term corrections [40] were applied on all oxides to treat the long range electrostatic interactions. The thermodynamic stability of a selection of structures were evaluated with other functionals (PBE + U [41], LDA + U [42], SCAN [43] and HSE06 [44, 45]) using the VASP code and Hubbard U for Ni was kept at 6 eV. All structures were optimized in the same functional as that for the final static (property) calculations. The screening parameter $\omega = 0.207$ Å^{-1} was consistently used for all HSE06 calculations. The energy cutoff for different functionals were specified in table S2. The PAW pseudopotentials (version LDA 5.4) of Li_*sv*, Ni_*pv* and O were used for the LDA + U calculations. For thermodynamically stable phases, the atomic chemical potentials ranges that a target phase is stable were determined using CPLAP [46, 47]. The average voltages and voltage profiles were calculated using the FM ordering spin arrangements using the PBEsol + U functional, since the magnetic ordering generally gives small differences to the calculated voltages. More details on the voltage calculations can be found on the "Voltage calculations" section in the supplementary information document. The band gaps were obtained from the HSE06 calculations. The climbing image NEB method [48, 49] was used to study Li-ion diffusion in $Li_2Ni_2O_3$. A 4 × 4 × 2 supercell (224 atoms) was used to ensure that the periodic image of the migrating Li is at least 12 Å apart. Additional electrons have been added to supercells to avoid the complexity associated with charge localization upon incorporating the Li vacancies.

The ase [50], pymatgen [51] packages were used for manipulating structures and general analysis. Sumo [52, 53] was used for plotting electronic and phonon band structures. The AiiDA framework [54, 55] was used to manage calculation provenance. Crystal structure diagrams were produced using VESTA [56].

3. Results and discussions

3.1. Re-exploring known systems

We initially performed searches on compositions with experimental structures. This ensures that sensible parameters were used to operate AIRSS effectively. We used the species pair-wise minimum separations, averaged volume per atom from known structures and symmetry to bias the search towards 'chemically sensible regions' enriched with low energy structures [22]. To validate the searches, we compare our searched structures with experimental structures that were optimized under identical settings. We also considered theoretical structures from materials project (MP) database [57, 58] in the analysis, although it is unclear how these structures were generated [23].

3.2. $LiNiO_2$

The layered $LiNiO_2$ structure is based on the ccp layers of oxygen anion lattice, with Li and Ni occupying in the octahedral sites, and was initially identified as an isostructural compound to the $R\bar{3}m$ $LiCoO_2$ cathode [6]. The (low spin) $t_{2g}^6e_g^1$ configuration of Ni^{3+} leads to pronounced Jahn-Teller (JT) distortions, resulting in larger volume changes during cycling compared to the layered $LiCoO_2$ [59]. Since it is demanding to capture the dynamic JT distortion experimentally, the layered $LiNiO_2$ structure has commonly been described as an average high symmetry $R\bar{3}m$ structure, with six identical Ni–O bond lengths [60]. First-principles studies identified a few distorted $LiNiO_2$ structures and several studies found the $P2_1/c$ structure with JT distorted octahedra arranged in a zigzag fashion as the ground state [6, 60–62]. The bond lengths of the distorted structure agree with the extended x-ray absorption fine structure data, which showed two sets of distinct bond lengths of 1.91 Å and 2.09 Å [63]. The $R\bar{3}m$ structure, on the other hand, is not dynamically stable and gives an erroneous electronic structure (i.e. showing a half-metal rather than a small band gap semiconductor) [62, 64–66]. Therefore, it is important to use the correct ground state structure in computational studies.

We performed searches using the minimum separations from the experimental average high symmetry $R\bar{3}m$ structure and the ground state $P2_1/c$ structure separately (see table S3) and notably both cases found the $P2_1/c$ as the ground state structure. The distribution of structures optimized from refined search is shown in figure 2. The energy ordering of the frequently mentioned $LiNiO_2$ structures relative to the ground state $P2_1/c$ structure follows: $C2/m$ ($+2.54$ meV atom^{-1}) $<$ $R\bar{3}m$ ($+28.17$ meV atom^{-1}), consistent with previous studies [60–62, 64]. A low energy distorted spinel-like structure ($+0.31$ meV atom^{-1}) was encountered by AIRSS (figure S1). This structure was also identified by a previous computation study and the parent undistorted spinel-like structure was seen in low-temperature synthesis of $LiCoO_2$ [62, 67]. Many other higher energy structures were also encountered by AIRSS, and some have lower predicted energies than the theoretical structures from the MP database. Most of the AIRSS structures have Ni in the distorted octahedral coordination and Li in octahedral or prismatic coordination. Overall, this search shows that AIRSS is an effective tool for exploring compounds that exhibit dynamic JT distortion.

3.3. Li_2NiO_3

Li_2NiO_3 is a Li-excess system, where Ni is (theoretically) in the $+4$ oxidation state, with electrochemistry driven by anionic redox. It is isostructural to Li_2MnO_3, with a ccp oxygen sublattice and alternating layers of pure Li and $[Ni_{2/3}Li_{1/3}]$ [8, 9, 11, 68]. The Li_2NiO_3 structure has been previously assigned to space groups $C2/m$ with 2 f.u. and $C2/c$ with 4 f.u., respectively [9]. We relaxed both the $C2/m$ and $C2/c$ structures and they give identical energies, confirming that they are identical ground state structures (figure 3). The ground state structures can also be accessed by AIRSS. An unreported low energy dynamically stable polymorph ($+1.10$ meV atom^{-1}) with a rock salt framework was also encountered (figure S2). AIRSS also found many other higher energy polymorphs and most of them are rock salts.

3.4. Li_2NiO_2

Assuming $2e^-$ (Ni^{2+}/Ni^{4+}) redox, the Li_2NiO_2 composition gives a high theoretical capacity (table 2). There are two Li_2NiO_2 experimental structures (figure 4): (1) $Immm$ Li_2NiO_2 (I-Li_2NiO_2), (2) $P\bar{3}m1$ Li_2NiO_2 (1T-Li_2NiO_2). The I-Li_2NiO_2 is isostructural to the orthorhombic Li_2CuO_2, and can be described as a structure with chains of edge-shared square planar $[NiO_4]$ units that is not based on close-packed oxygen layers [69, 70]. The 1T-Li_2NiO_2 structure has oxygen anions arranged in hexagonal close-packed (hcp)

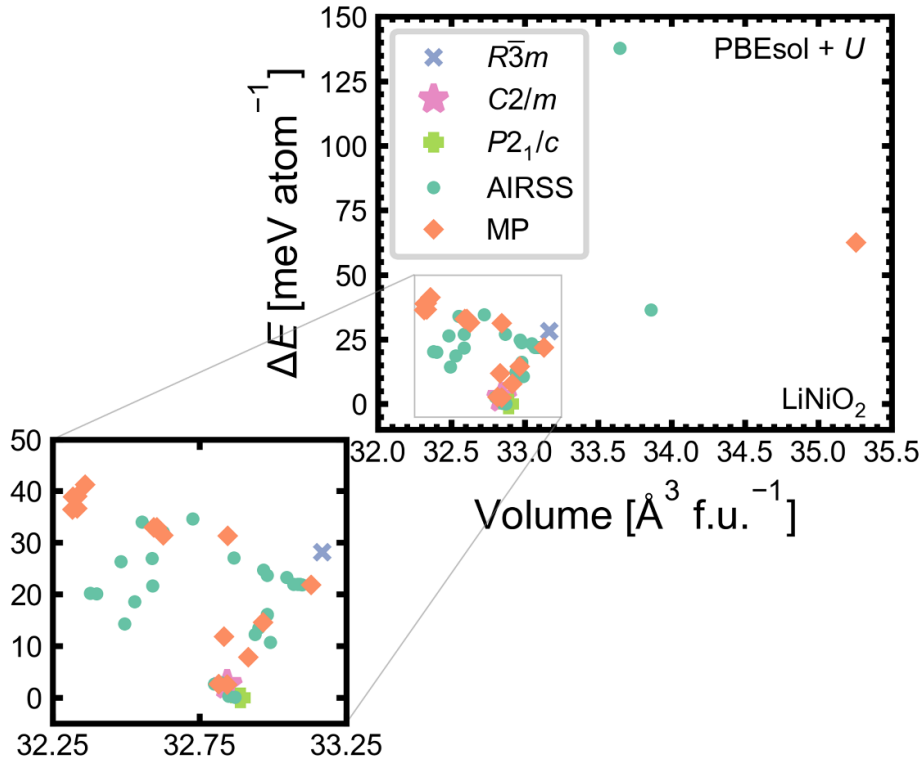

Figure 2. Energy vs volume plot for the low energy $LiNiO_2$ structures optimized with the PBEsol + U functional. The legend shows the three reference structures in the corresponding space groups. Structures from materials project (MP) database are represented by diamonds and those encountered by AIRSS are labelled by circles.

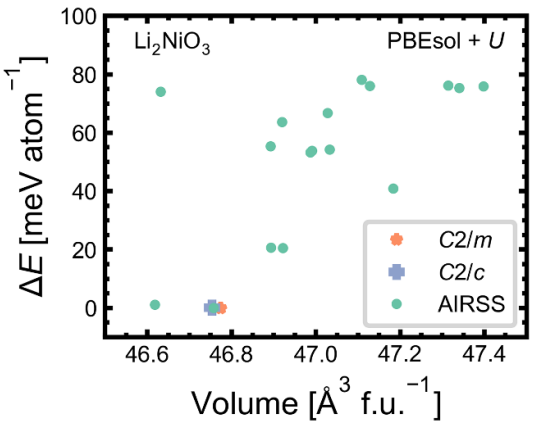

Figure 3. Energy vs volume plot for the low energy Li_2NiO_3 structures optimized with the PBEsol + U functional. The legend shows the two reference experimental structures in the corresponding space groups. Structures encountered by AIRSS are labelled by circles.

layers, with layers of Ni in octahedral sites and layers of Li in tetrahedral sites distributing between the oxygen layers alternately [71]. The ground state Li_2NiO_2 structure is the I-Li_2NiO_2 as heating the 1T-Li_2NiO_2 gives I-Li_2NiO_2. [70] While I-Li_2NiO_2 can be accessed by solid-state synthesis method, the metastable 1T-Li_2NiO_2 can hardly be synthesized via solid-state reaction directly [69, 72]. The unfavorable electrostatic repulsion between the tetrahedrally coordinated Li was considered as the primary factor in affecting their stability ordering [69]. The minimum separations between Li are 2.48 Å and 2.28 Å for the optimized structures of I-Li_2NiO_2 and 1T-Li_2NiO_2, respectively (see figure S3). The latter structure has Li more closely packed, giving greater repulsion.

The energy ordering of the I-Li_2NiO_2 and 1T-Li_2NiO_2 phases predicted by DFT at 0 K varies with choices of functionals. The PBEsol + U and HSE06 results suggest that the 1T-Li_2NiO_2 phase is the ground state, whereas results from the SCAN functional indicate that the I-Li_2NiO_2 is the ground state (table 3). The energy difference between the FM ordering and antiferromagnetic ordering (AFM) of 1T-Li_2NiO_2 is

Table 2. Properties of known Li-Ni-O structures and the lowest energy dynamically stable AIRSS discovered structure. Average voltages (V_{avg}), volume changes relative to the fully lithiated phase (ΔVolume) during Li extraction and theoretical energy densities were calculated with PBEsol + U on the ferromagnetic ordering cell and assuming only cationic redox (thus properties of structures with electrochemistry driven purely by anionic redox (e.g. Li_2NiO_3) are not shown here). Band gaps were obtained from HSE06 calculations using the HSE06 optimized structures with ground state magnetic ordering. Space group detection was carried out using a symmetry tolerance of 1×10^{-2}.

Space group	Formula	Formal oxidation state on Ni	Theoretical energy density (W h kg^{-1})	Theoretical capacity (mAh g^{-1})	V_{avg} (V)	ΔVolume (%)	Band gap (eV)
Immm	Li_2NiO_2	+2	1728.71	512.58	3.37	−17.94	3.87
$P\bar{3}m1$	Li_2NiO_2	+2	1629.69	512.58	3.18	−13.58	5.00
$R\bar{3}m$	Li_4NiO_3	+2	1598.36	398.67	4.01	−8.37	5.10
$P2_1/c$	$LiNiO_2$	+3	1065.92	274.51	3.88	−8.61	2.06
$R\bar{3}m$	$Li_2Ni_2O_3$	+2	1053.64	299.01	3.52	−11.38	5.03
$P2_1/m$	Li_6NiO_4	+2	920.69	326.18	2.82	−7.18	4.82
$P\bar{1}$	$Li_4Ni_2O_5$	+3	734.17	238.08	3.08	−7.83	2.61
$P\bar{1}$	$Li_2Ni_3O_4$	+2	624.52	211.07	2.96	−11.06	2.87
$C2/c$	Li_3NiO_3	+3	553.78	210.18	2.63	−26.38	2.94
$P\bar{1}$	Li_5NiO_4	+3	490.64	170.28	2.88	−18.77	3.06
$C2/m$	$Li_2Ni_4O_5$	+2	475.22	163.10	2.91	−8.78	3.12
$P1$	$LiNi_3O_5$	+3	430.75	101.90	4.23	−3.53	0.66

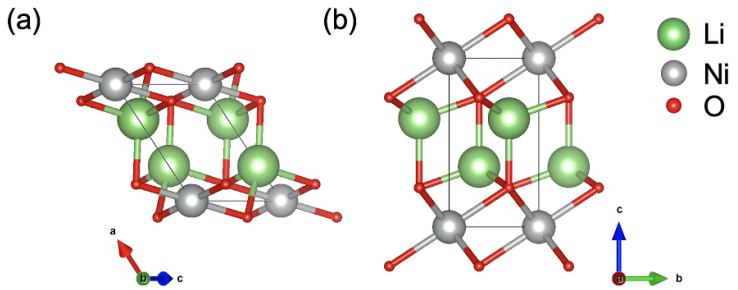

Figure 4. The two experimental Li_2NiO_2 structures: (a) *Immm* Li_2NiO_2 (I-Li_2NiO_2); (b) $P\bar{3}m1$ Li_2NiO_2 (1T-Li_2NiO_2).

Table 3. The energy difference (ΔE) relative to the lowest energy phase calculated using the PBEsol + U, HSE06 and SCAN functionals separately for the *Immm* Li_2NiO_2 (I-Li_2NiO_2) and $P\bar{3}m1$ Li_2NiO_2 (1T-Li_2NiO_2). The ferromagnetic (FM) and antiferromagnetic (AFM) spin states were considered for the magnetic 1T-Li_2NiO_2. The I-Li_2NiO_2 is non-magnetic (NM).

	ΔE (meV $atom^{-1}$)		
Theory	PBEsol + U	HSE06	SCAN
I-Li_2NiO_2 (NM)	58.27	10.95	0.00
1T-Li_2NiO_2 (AFM)	0.00	0.00	4.27
1T-Li_2NiO_2 (FM)	0.17	0.11	4.59

negligible. However, the AFM ordering is always lower in energy than that of the FM ordering, which is consistent with its magnetic behavior at low temperatures [71]. Despite that the energy ordering at 0 K does not necessarily equate to the energy ordering observed in experiments at some finite temperatures, the discrepancies between different functionals partly originate from the inherent limitations of DFT in approximating electron interactions and the Hubbard U plays a role in biasing the results [28, 44, 45, 73, 74]. Using the PBEsol + U functional, the predicted ground state structure is I-Li_2NiO_2 when $U = 0$–4 eV, however, the 1T-Li_2NiO_2 becomes lower in energy when $U > 4$ eV (figure S4).

We also considered the lattice dynamics in both phases and evaluated the vibrational contribution to the constant volume Helmholtz free energy (A) using the PBEsol + U functional to predict the thermodynamic stability following [75]:

$$A(T) = U^{\text{latt}} + U^{\text{vib}}(T) - TS^{\text{vib}}(T). \quad (1)$$

U^{latt} is the athermal lattice energy. U^{vib} and S^{vib} denote the vibrational internal energy and vibrational entropy from phonon contribution under the harmonic model, respectively. Figure S5 shows the Helmholtz free energy difference ΔA relative to the lower energy phase as a function of temperature. Between 0 and

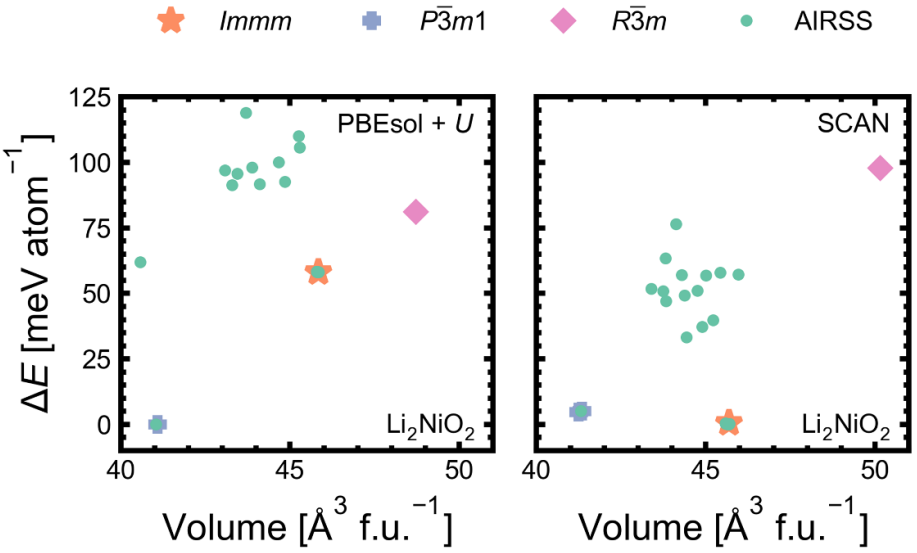

Figure 5. Energy vs volume plot for the low energy Li_2NiO_2 structures optimized with the PBEsol + U and SCAN functionals. The legend shows the three reference structures in their corresponding space groups. The *Immm* and $P\bar{3}m1$ phase are experimental structures whereas the $R\bar{3}m$ phase is a theoretical structure from the materials project (MP) database. Structures encountered by AIRSS are labelled by circles.

1000 K, the 1T-Li_2NiO_2 is always lower in energy and higher temperature gives greater stabilization over the I-Li_2NiO_2 phase. Therefore, this method failed to describe the phase stability of Li_2NiO_2 or to predict any temperature-induced phase transitions with the chosen functional. Some forms of anharmonicity (e.g. associated with the square planar [NiO_4] geometry), may have been neglected in the calculations.

Although there exist two experimental Li_2NiO_2 phases with distinctive structural framework, we simply use the minimum separations from Li_2NiO_3 to perform the search (table S3). This is an example of an explorative search, where the structural information from a relevant composition is used to generate sensible random structures. Regardless of the oxidation states on Ni, the minimum separations from different ($Li_xNi_yO_z$) compositions set constraints that avoid cation-cation and anion-anion being too close, hence the separations do not need to be exact values to achieve efficient searching. Figure 5 shows the structures optimized using the PBEsol + U and SCAN functionals. Both the I-Li_2NiO_2 and 1T-Li_2NiO_2 phases were encountered by AIRSS. We also identified two higher energy polymorphs and phonon calculations showed that they are located at local energy minima (figures S6 and S7).

3.5. Exploring new systems

Table 1 shows the 11 new systems performed with explorative searches according to the pair-wise minimum separations from table S3. Further property calculations (e.g. band gaps, average voltages) were performed on dynamically stable structures (see figure S12) with distances to the convex hull of the Li-Ni-O phase diagram within 100 meV $atom^{-1}$ (i.e. $E_{above\_hull} < 100$ meV $atom^{-1}$) from PBEsol + U calculations, as the chosen energy range generally covers that for experimental synthesizable structures [76].

From table 1, $Li_2Ni_2O_3$ is a thermodynamically stable phase on the Li-Ni-O convex hull. The next low energy phase is the metastable Li_4NiO_3, with $E_{above\_hull} < 10$ meV $atom^{-1}$. Interestingly, the structures of $Li_2Ni_2O_3$ and Li_4NiO_3 (see figure 6) resemble 1T-Li_2NiO_2 (figure 4(b)). In $Li_2Ni_2O_3$, for every layer of (tetrahedral) Li and there are two (octahedral) Ni layers arranged repeatedly. The Li_4NiO_3 structure, however, has two Li layers for every Ni layer. The additional layering of Li in Li_4NiO_3 gives more unfavorable electrostatic repulsion, making the structure less stable. Overall, there is a consistent energy (E_{above_hull}) ordering of phases predicted using the PBEsol + U and HSE06 functionals. The HSE06 functional tends to better describe the electronic structures for a wider range of materials in different chemical environments and hence their results are generally more reliable [44, 45].

Assuming only cationic redox during delithiation, the average voltages, theoretical capacities and theoretical energy densities for dynamically stable phases are benchmarked against experimentally known phases (table 2). The two Li_2NiO_2 phases have the highest theoretical energy densities, suggesting that they are potentially good cathode candidates. Unfortunately, the practical performance of I-Li_2NiO_2 is poor, as it was found to experience an irreversible structural change and a significant capacity loss during the first charge–discharge cycle [69]. The 1T-Li_2NiO_2, on the other hand, was reported to be stable over 100 cycles

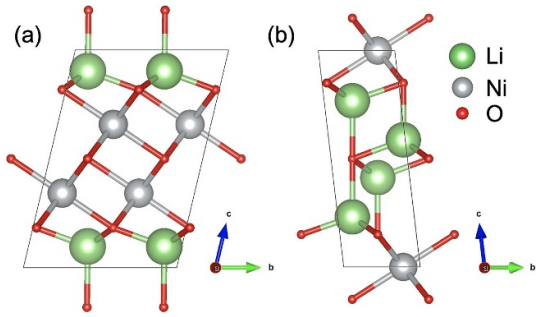

Figure 6. The structures of the (a) thermodynamically stable $R\bar{3}m$ $Li_2Ni_2O_3$ and (b) metastable $R\bar{3}m$ Li_4NiO_3 phase encountered by AIRSS.

between 1.7 and 4.0 V, despite the voltage hysteresis [70]. Below half lithiation, the 1T-Li_2NiO_2 becomes the layered $LiNiO_2$, and its practical performance is limited due to the existing issues with cycling $LiNiO_2$ (e.g. the anisotropic lattice change and the various phase transformations during lithium deintercalation) [6, 8, 77, 78].

For layered intercalation cathode materials, volume reductions (>5%) are commonly observed when >75% of Li have been extracted from the structures [79]. The cell volume change at different Li contents has contributions from: (1) steric factors (e.g. the number of Li that are required to sterically sustain the interlayer spacing); (2) electrostatic factors (e.g. strength of Van der Waals interactions vs other coulombic interactions) [80]. The experimental percentage volume reduction for the layered $LiNiO_2$ to the H3 phase (approaching a dilute limit of Li) is around 7%, which is close to the calculated result [6]. Structures with layers of tetrahedral Li generally have a larger volume reduction than those with octahedral Li (e.g. the layered $LiNiO_2$ vs 1T-Li_2NiO_2), as the Li slab thickness (see table S4) is generally greater for structures with layers of tetrahedral Li to accommodate additional Li.

The I-Li_2NiO_2 experiences a greater volume change compared the 1T-Li_2NiO_2, and their Ni coordination can explain this. Kang *et al* [69] indicated that the square planar [NiO_4] coordination in I-Li_2NiO_2 is extremely unfavorable in the delithiated state, which led to structural collapse upon cycling. Significant volume changes (>17%) are also observed on the Li_3NiO_3 and Li_5NiO_4 phases, where Ni coordination is exclusively based on square planar/bipyramid. According to the crystal field theory, electron configurations of d^7 low spin (Ni^{3+}) and d^8 (Ni^{2+}) would encourage square planar Ni. However, there are only few experimental structures with Ni in square planar coordination. Many ternary Li-Ni-O compounds are in either the layered or rock salt framework [6, 9]. The preference for Ni to adopt in the square planar coordination is therefore not greatly driven by the crystal field stabilization energy but other (long range) electrostatic interactions between the ions [69]. At a high Li content, square planar Ni provides greater stabilization by increasing the separation between the Li. When some Li are removed from the structure, the driving force for Ni to adopt in the square planar coordination to stabilize the structure is reduced and octahedral NiO_6 becomes more favorable. Consequently, structures with square planar Ni can transform more easily, leading to irreversible structural change and large volume change.

The electronic conductivities generally decrease with increasing band gaps. The band gaps of 1T-Li_2NiO_2, $Li_2Ni_2O_3$ and Li_4NiO_3 are $\geqslant$5 eV (see table 2), suggesting that the structural feature of layers of tetrahedral Li^+ and octahedral Ni^{2+} is associated with poorer electronic conductivity. Previous studies indicated that the charge transfer mechanism in layered $LiNiO_2$ are dominated by small polaron hopping mechanisms [13, 81]. The electron transport in similar materials can be further calculated using the small polaron migration model [82].

From the projected density of states of the ternary Li-Ni-O phases calculated with HSE06 functional (figures S13–S15), the valence band maxima (VBM) of all phases are composed of Ni 3*d* states and O 2*p* states, and the conduction band minima are dominated by Ni 3*d* states. Since late 3*d* TM tend to have increased bonding with oxygen (i.e. more hybridized), the contribution of O states at VBM are generally higher compared to other compounds (e.g. $LiCoO_2$) [81]. There is a general trend that O states contribution increases with the formal oxidation states of Ni. The proportion of O states at the VBM for a given Li-Ni-O phase could indicate its oxygen thermal stability and the potential for anionic redox. Materials with electrochemistry driven by anionic redox (e.g. Li_2NiO_3) generally have poorer oxygen thermal stability [8, 9]. The larger O states contribution of 1T-Li_2NiO_2 at the VBM compared to that of I-Li_2NiO_2 could be related to the poorer oxygen thermal stability of 1T-Li_2NiO_2.

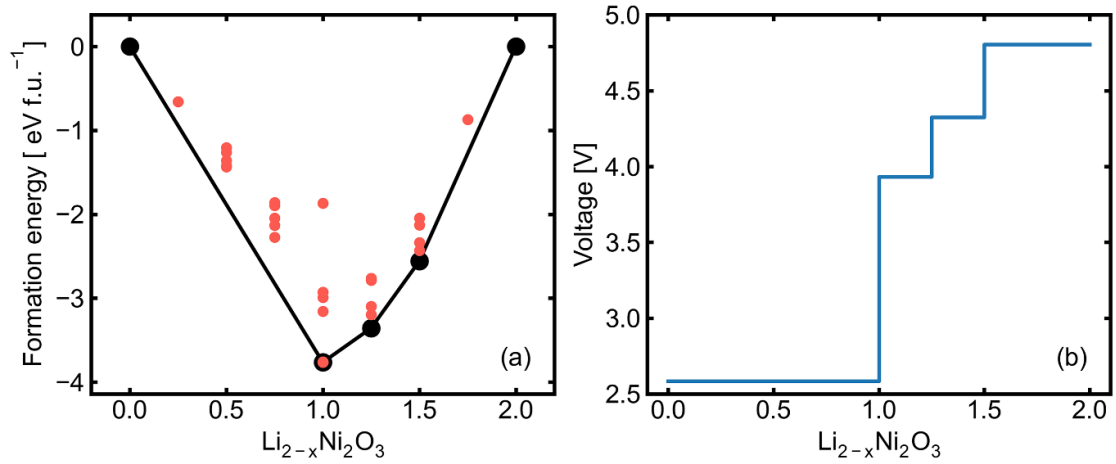

Figure 7. (a) The convex hull of delithiated $Li_{2-x}Ni_2O_3$ structures calculated using the PBEsol + U functional; (b) voltage profile constructed from the convex hull.

Overall, the layered $Li_2Ni_2O_3$ and Li_4NiO_3 have comparable and/or better theoretical capacity and energy density to $LiNiO_2$. The volume shrinkage behavior could be improved by elemental substitution [6, 79]. Depending on the site preference of the extrinsic species on the host, foreign species with a large ionic radius (e.g. Mg^{2+}, W^{6+}) could act as a pillaring ion which either sit on the Li/Ni layers to reduce the shrinking of the Li/Ni layers [83, 84]. The structural instability induced by the JT effect due to the formation of Ni^{3+} during delithiation can also be alleviated by introducing impurities [79].

3.6. The properties of $Li_2Ni_2O_3$

3.6.1. Electrochemical properties

The convex hull shown in figure 7(a) was constructed by calculating all the unique configurations of delithiated structures over all the Li content in a $2 \times 2 \times 1$ supercell with four formula units of $Li_2Ni_2O_3$. There are three stable intermediate phases and the structures on the convex hull of the $Li_2Ni_2O_3$–Ni_2O_3 phase diagram are shown in figure S16. The shape of the convex hull suggests a two-phase transition between the $Li_2Ni_2O_3$ ($x = 0$) and $LiNi_2O_3$ ($x = 1$). The intermediate $LiNi_2O_3$ phase (figure S16(b)) has a layer of octahedral Li, analogous to that in $LiNiO_2$. Therefore, the tetrahedral Li arrangement (in $Li_2Ni_2O_3$) is for accommodating additional Li in the structure. A precursor to prepare the $Li_2Ni_2O_3$ could be the layered $LiNi_2O_3$ phase with octahedral Li.

To verify the existence of the layered $LiNi_2O_3$ structure, we performed AIRSS search on this mix-valent composition. This structure, which exists in the $P\bar{3}m1$ space group, was encountered by AIRSS. Figure S17 shows that it is at a local energy minimum. Interestingly, the lowest energy structure with the $LiNi_2O_3$ composition is not the $P\bar{3}m1$ $LiNi_2O_3$, and the energy difference between the $P\bar{3}m1$ $LiNi_2O_3$ and the lowest energy $Immm$ $LiNi_2O_3$ structure is 27.63 meV atom^{-1}. Within this energy difference window, there also exist several polymorphs. Some of the polymorphs are layered, with pure NiO_6 octahedra arranged in a single layer of rather than two consecutive layers as in $Li_2Ni_2O_3$. This suggests that the structural feature of NiO_6 units arranged in two consecutive layers is stabilized by excess Li.

Figure S18 shows the volume change for the $Li_{2-x}Ni_2O_3$ lattice on the convex hull. The volume decreased rapidly between $x = 0 \rightarrow 1$. This has contributions from the decreasing thickness of the Li layers and the shortening of Ni–O bond due to Ni oxidation. There exists a small window ($1.0 < x < 1.5$) with small volume variation, but further Li extraction collapses the Li layer. The final delithiated Ni_2O_3 is not thermodynamically stable structure on the Li-Ni-O convex hull, with $E_{\text{above\_hull}} = 264.88$ meV atom^{-1} according to PBEsol + U calculations. The $Cmcm$ Ni_2O_3 phase from the MP database is lower in energy by 9.15 meV atom^{-1}.

Figure 7(b) shows that the average potential window is between 2.6 and 4.8 V, but the low voltage part dominates, which is not a desirable feature for a cathode. We note that the calculated voltages may contain systematic errors, since the voltages from DFT calculations is sensitive to the choice of functional and that not all the structural transformations can be captured or correctly predicted [22].

3.6.2. Li diffusion

Ionic conductivities in intercalation cathodes (e.g. $LiNiO_2$) are mostly governed by the mobility of Li^+ [13]. The Li slab thickness, the electrostatic interactions between diffusing ions and the surrounding cations are

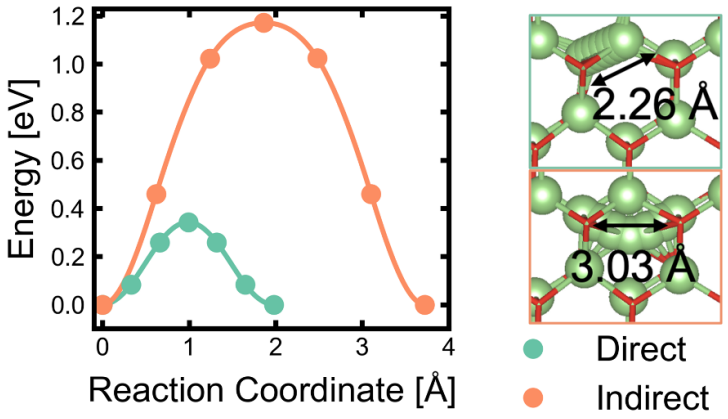

Figure 8. The energy profiles for a Li to diffusion along the direct (green frame) and indirect (orange frame) paths in a supercell with a single Li vacancy. Zoomed in crystal structures only show the green Li atoms and red Li–O bonds for clarity.

considered to greatly influence ion mobility [59, 85]. Despite the fact that Li slab thickness is increased in Li-excess systems (e.g. 1T-Li_2NiO_2) to hold more Li (see table S4), it was speculated that Li diffusion is not promising as the overall available space for diffusion is reduced [72]. The electrostatic repulsion between more closely arranged Li is a contributing factor [8, 86].

To estimate the activation energies for Li migration in $Li_2Ni_2O_3$, we identified two plausible diffusion paths with a supercell containing a single Li^+ vacancy: (1) a direct hop from one tetrahedral site to the nearest neighboring tetrahedral site, with a hopping distance of 2.26 Å; (2) an indirect hop from one tetrahedral site to the next nearest tetrahedral site (∼3.03 Å away) via an interstitial site that is ∼1.68 Å away from the initial/end positions of the diffusing Li. Figure 8 shows that a direct hop between the nearest Li tetrahedral sites is more favorable, with a barrier height of 0.34 eV. The direct hop maximizes the distance between the diffusing Li with the surrounding Li, therefore minimizes the unfavorable electrostatic/steric contributions from closely arranged Li.

We also considered divacancy-like migration paths by introducing two vacancies in the supercell [87]. The energy of the configuration with two clustered Li vacancies (∼2.26 Å apart) is (∼0.40 eV) higher than that with two vacancies being ∼3.03 Å apart (figure S19). Nevertheless, the energy barrier for a Li^+ to hop directly to a vacant site is lower than that of an indirect hop. The barrier height for the divacancy indirect hop is 0.17 eV lower than that of the monovacancy case and we attribute this reduced barrier to the lowering of electrostatic repulsion between fewer adjacent Li and the diffusing Li^+. The barrier for Li^+ diffusion would theoretically decrease further when the system approaches a more Li dilute limit. However, this assumes that the structures remain stable in their highly delithiated states.

3.6.3. The stability field of $LiNiO_2$

We have discussed the properties of predicted structures for battery cathode applications. A new stable structure, however, may have implications beyond its properties. Here, we use an example to demonstrate how previously undiscovered stable phases can be used explain the chemistries of other related phases.

The synthesis-defect chemistry-property relationships of several complex oxide battery cathode materials have been investigated by theoretical studies [81, 88]. One key term for calculating the defect formation energies is the atomic chemical potential, which can be considered as the available atomic species responsible for generating the defects [88]. The ranges of atomic chemical potentials where the target compound is stable reflect the ranges of possible growth environments for the material to be synthesized experimentally. Under the assumption that a ternary compound $Li_xNi_yO_z$ forms in an equilibrium reaction with constituent elements' standard phases requires

$$x\mu_{\mathrm{Li}} + y\mu_{\mathrm{Ni}} + z\mu_{\mathrm{O}} = \Delta H_{\mathrm{f}}\left(\mathrm{Li_xNi_yO_z}\right), \tag{2}$$

to be satisfied, where ΔH_{f} is the formation enthalpy. To avoid decomposition to the elemental phases, $\mu_{\mathrm{Li}} \leqslant 0$, $\mu_{\mathrm{Ni}} \leqslant 0$ and $\mu_{\mathrm{o}} \leqslant 0$ are required. The competing phases impose additional thermodynamic constraints. For example, to avoid the formation of NiO: $\mu_{\mathrm{Ni}} + \mu_O \leqslant \Delta H_{\mathrm{f}}(\mathrm{NiO})$. For a system containing n number of species with m competing phases, combinations of $n-1$ linear equations are solved at one time from a total of $2n+m-1$ equations automatically using CPLAP [47]. Only solutions that simultaneously

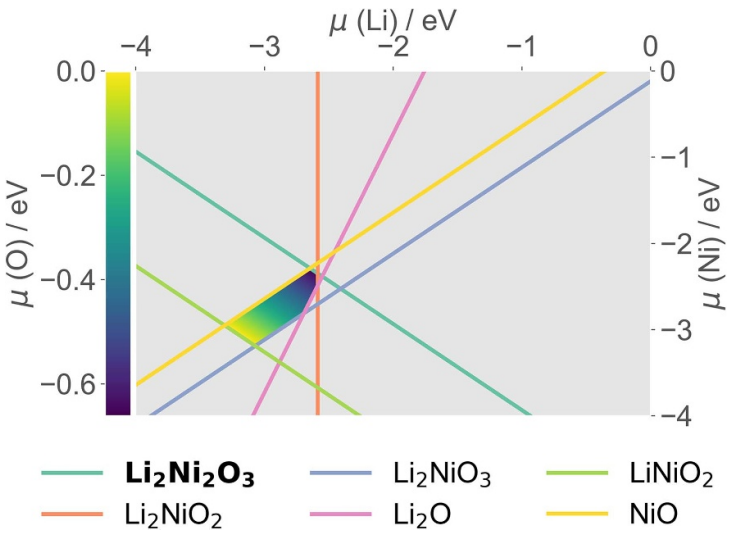

Figure 9. The resulting chemical potential stability region (colored region) of $LiNiO_2$ due to the limits imposed by the formation of five competing phases, calculated using the HSE06 functional. The new $Li_2Ni_2O_3$ phase is highlighted in bold.

satisfy the conditions given by all constraints are kept. The final solutions yield a region of stability in the plane defined by the independent variables μ_{Li} and μ_{Ni}. A large atomic chemical potential stability field corresponds to a wider range of growth environments for the host. The defect formation energies, therefore, can vary over a larger range. Since defect concentrations scale exponentially with the defect formation energies, the predicted concentrations can be orders of magnitude different. To correctly calculate the atomic chemical potentials term, it is essential to consider all the stable phases in the corresponding phase diagrams [47].

Hoang and Johannes presented a detailed DFT study on the intrinsic point defects for the layered $LiNiO_2$ [13]. Their atomic chemical potential diagram shows that the thermodynamic stability window of $LiNiO_2$ is constrained by four other limiting phases, which gives five unique sets of atomic chemical potentials. We re-evaluated the stability field of $LiNiO_2$ by incorporating the $Li_2Ni_2O_3$ phase in the calculations. Figure 9 shows that $Li_2Ni_2O_3$ is an additional limiting phase which affects the thermodynamic stability of $LiNiO_2$. We repeated the analysis using several other functionals (LDA + U, PBE + U, PBEsol + U, SCAN) and all calculations (see figure S20) suggest the $Li_2Ni_2O_3$ is a limiting phase for $LiNiO_2$, despite that it is yet a hypothetical structure. Therefore, the defect chemistry of $LiNiO_2$ could potentially be different.

3.6.4. The likelihood of synthesizing AIRSS predicted phases

Our calculations have revealed the structures of many (meta-)stable Li-Ni-O compounds. However, the experimental synthesis of those compounds may be challenging (e.g. require out-of-equilibrium conditions) or impossible. It is likely that the predicted phases exist in the disordered forms due to the cation mixing behaviors of Li/Ni. The predicted phase stability at 0 K does not account for temperature effects which also encourage disordering. The challenges of getting a precise control of the known compositions/structures in the Li-Ni-O phase space have also been discussed in previous works [6, 9]. We tried to incorporate finite temperature effects in our PBEsol + U convex hull analysis. This includes computing the constant volume Helmholtz free energies from phonon calculations (see figure S21), where the entropy term of O_2 gas was taken from the thermochemical tables [89]. Additionally we estimated the Gibbs free energies using the machine-learned descriptor (see figure S22) [90]. Unfortunately, neither approaches correctly capture the stability of known phases. The DFT + U method, with U calibrated to materials properties (e.g. band gaps, oxidation enthalpies) are limited known experimental phases such as NiO and NiO_2. Therefore, more advanced theoretical methods (e.g. linear response calculations of DFT + $U(+V)$ with onsite U (and intersite V) term determined self-consistently) may be needed to improve the phase stability prediction [30, 91–94].

Finally, we evaluated the thermodynamic stability of $Li_2Ni_2O_3$ using HSE06 (see figure 10), LDA + U, PBE + U, PBEsol + U and SCAN functionals (see figure S23). The narrow stability field suggests the difficulty in synthesizing this compound. It is predicted to form under an extremely O-poor and Li-rich environment. The limiting phases are $LiNiO_2$, 1T-Li_2NiO_2/I-Li_2NiO_2 and NiO (figure 10).

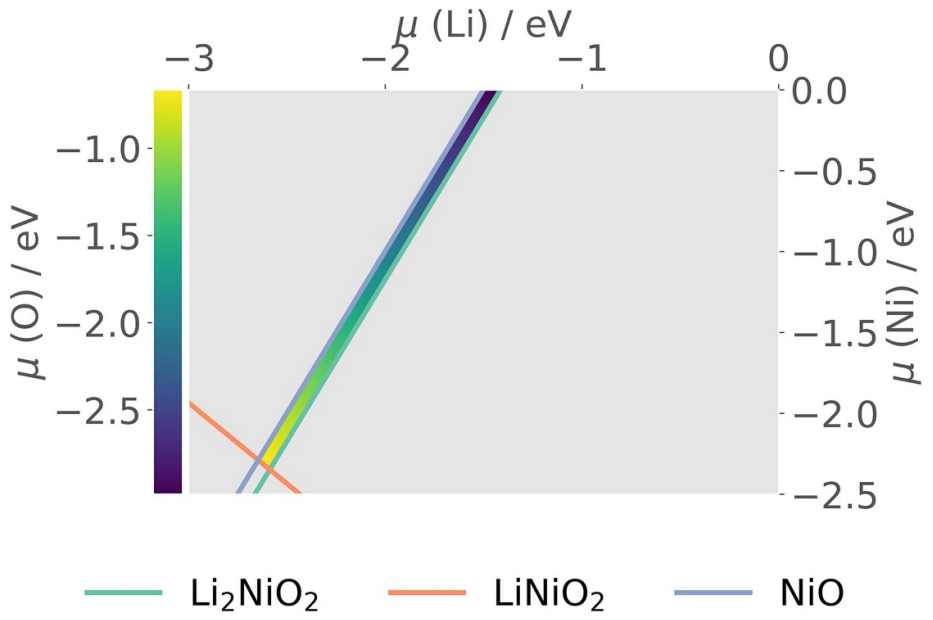

Figure 10. The chemical potential stability region (colored region) of $Li_2Ni_2O_3$, calculated using the HSE06 functional.

4. Conclusions

We have explored $Li_xNi_yO_z$ in the Li-Ni-O phase diagram and predicted many (meta-)stable structures using AIRSS. The $LiNiO_2$ search shows the capability of AIRSS to explore structures displaying dynamic JT distortions. The predicted energy ordering of known Li_2NiO_2 phases is sensitive to the choice of density functionals and Hubbard *U*. Among the low energy $Li_xNi_yO_z$ structures, Ni can adopt octahedral and square planar/bipyramid coordination, with octahedral coordination being the most common. Previously unknown thermodynamically stable layered $Li_2Ni_2O_3$ and metastable layered Li_4NiO_3 ($<$10 meV atom^{-1} above the hull), are predicted to have comparable theoretical energy densities to the layered $LiNiO_2$ and both have layers of octahedral Ni and edge-sharing tetrahedral Li to accommodate excess Li, like that in 1T-Li_2NiO_2. The structural feature is associated with a large band gap ($\sim$5 eV) and large volume change upon delithiation. Li diffusion in $Li_2Ni_2O_3$ would take place along paths that are farthest to the surrounding Li^+ to minimize electrostatic repulsion. Several density functionals consistently predicted that the $Li_2Ni_2O_3$ phase further reduces the thermodynamic stability ranges of $LiNiO_2$, which is known to be difficult to be synthesized stoichiometrically. By revealing the structures and properties of our predicted phases, these phases may become more identifiable in future experiments. Finally, we show that structure prediction is a valuable approach to explore the chemical space with complex chemistry.

Data availability statement

The data that support the findings of this study are openly available at the following URL/DOI: https://doi.org/10.5281/zenodo.8022111 [95].

Acknowledgments

This work was supported by the Faraday Institution Grant No. FIRG017 and used the Michael supercomputer (FIRG030). Via our membership of the UK's HEC Materials Chemistry Consortium, which is funded by the UK Engineering and Physical Sciences Research Council EPSRC (EP/L000202, EP/R029431, EP/T022213), this work used ARCHER2 UK National Supercomputing Services. We are also grateful to the UK Materials and Molecular Modelling Hub (MMM Hub), which is partially funded by the EPSRC (EP/P020194/1, EP/T022213/1), for computational resources on the Thomas, Young supercomputers, and to UCL for access to the Myriad (Myriad@UCL) and Kathleen (Kathleen@UCL) supercomputers.

Author contributions

The manuscript was written through contributions of all authors. All authors have given approval to the final version of the manuscript.

Conflict of interest

The authors declare no conflicts of interest.

ORCID iDs

Jiayi Cen https://orcid.org/0000-0001-8208-1147
Bonan Zhu https://orcid.org/0000-0001-5601-6130
David O Scanlon https://orcid.org/0000-0001-9174-8601

References

[1] Manthiram A 2020 A reflection on lithium-ion battery cathode chemistry *Nat. Commun.* **11** 1550
[2] Palacín M R 2009 Recent advances in rechargeable battery materials: a chemist's perspective *Chem. Soc. Rev.* **38** 2565–75
[3] Liu C, Neale Z G and Cao G 2016 Understanding electrochemical potentials of cathode materials in rechargeable batteries *Mater. Today* **19** 109–23
[4] Ding Y, Cano Z P, Yu A, Lu J and Chen Z 2019 Automotive Li-ion batteries: current status and future perspectives *Electrochem. Energy Rev.* **2** 1–28
[5] Li M and Lu J 2020 Cobalt in lithium-ion batteries *Science* **367** 979
[6] Bianchini M, Roca-Ayats M, Hartmann P, Brezesinski T and Janek J 2019 There and back again—the journey of $LiNiO_2$ as a cathode active material *Angew. Chem., Int. Ed.* **58** 10434–58
[7] Yu L, Liu T, Amine R, Wen J, Lu J and Amine K 2022 High nickel and no cobalt─the pursuit of next-generation layered oxide cathodes *ACS Appl. Mater. Interfaces* **14** 23056–65
[8] Jia Y, Ye Y, Liu J, Zheng S, Lin W, Wang Z, Li S, Pan F and Zheng J 2022 Breaking the energy density limit of $LiNiO_2$: Li_2NiO_3 or Li_2NiO_2? *Sci. China Mater.* **65** 913–9
[9] Bianchini M *et al* 2020 From $LiNiO_2$ to Li_2NiO_3: synthesis, structures and electrochemical mechanisms in Li-rich nickel oxides *Chem. Mater.* **32** 9211–27
[10] Mesnier A and Manthiram A 2020 Synthesis of $LiNiO_2$ at moderate oxygen pressure and long-term cyclability in lithium-ion full cells *ACS Appl. Mater. Interfaces* **12** 52826–35
[11] Shinova E, Zhecheva E, Stoyanova R and Bromiley G D 2005 High-pressure synthesis of solid solutions between trigonal $LiNiO_2$ and monoclinic $Li[Li_{1/3}Ni_{2/3}]O_2$ *J. Solid State Chem.* **178** 1661–9
[12] Rougier A, Gravereau P and Delmas C 1996 Optimization of the composition of the $Li_{1-z}Ni_{1+z}O_2$ electrode materials: structural, magnetic, and electrochemical studies *J. Electrochem. Soc.* **143** 1168–75
[13] Hoang K and Johannes M D 2014 Defect chemistry in layered transition-metal oxides from screened hybrid density functional calculations *J. Mater. Chem.* A **2** 5224–35
[14] Shannon R D 1976 Revised effective ionic radii and systematic studies of interatomic distances in halides and chalcogenides *Acta Cryst.* A **32** 751–67
[15] Zheng J, Ye Y, Liu T, Xiao Y, Wang C, Wang F and Pan F 2019 Ni/Li disordering in layered transition metal oxide: electrochemical impact, origin, and control *Acc. Chem. Res.* **52** 2201–9
[16] Zheng J *et al* 2017 Role of superexchange interaction on tuning of Ni/Li disordering in layered $Li(Ni_xMn_yCo_z)O_2$ *J. Phys. Chem. Lett.* **8** 5537–42
[17] Li S, Shadike Z, Kwon G, Yang X-Q, Lee J H and Hwang S 2021 Asymmetric reaction pathways of conversion-type electrodes for lithium-ion batteries *Chem. Mater.* **33** 3515–23
[18] Oganov A R, Pickard C J, Zhu Q and Needs R J 2019 Structure prediction drives materials discovery *Nat. Rev. Mater.* **4** 331–48
[19] Pickard C J and Needs R J 2011 *Ab initio* random structure searching *J. Phys.: Condens. Matter* **23** 053201
[20] Pickard C J and Needs R J 2006 High-pressure phases of silane *Phys. Rev. Lett.* **97** 045504
[21] Booth S G *et al* 2021 Perspectives for next generation lithium-ion battery cathode materials *APL Mater.* **9** 109201
[22] Lu Z, Zhu B, Shires B W B, Scanlon D O and Pickard C J 2021 *Ab initio* random structure searching for battery cathode materials *J. Chem. Phys.* **154** 174111
[23] Zhu B, Lu Z, Pickard C J and Scanlon D O 2021 Accelerating cathode material discovery through *ab initio* random structure searching *APL Mater.* **9** 121111
[24] Zhu B and Scanlon D O 2022 Predicting lithium iron oxysulfides for battery cathodes *ACS Appl. Energy Mater.* **5** 575–84
[25] Davies D W, Butler K T, Jackson A J, Morris A, Frost J M, Skelton J M and Walsh A 2016 Computational screening of all stoichiometric inorganic materials *Chem* **1** 617–27
[26] Clark S J, Segall M D, Pickard C J, Hasnip P J, Probert M I J, Refson K and Payne M C 2005 First principles methods using CASTEP *Z. Kristallogr. Cryst. Mater.* **220** 567–70
[27] Perdew J P, Ruzsinszky A, Csonka G I, Vydrov O A, Scuseria G E, Constantin L A, Zhou X and Burke K 2008 Restoring the density-gradient expansion for exchange in solids and surfaces *Phys. Rev. Lett.* **100** 136406
[28] Dudarev S L, Botton G A, Savrasov S Y, Humphreys C J and Sutton A P 1998 Electron-energy-loss spectra and the structural stability of nickel oxide: an LSDA+U Study *Phys. Rev.* B **57** 1505–9
[29] Mueller T, Hautier G, Jain A and Ceder G 2011 Evaluation of tavorite-structured cathode materials for lithium-ion batteries using high-throughput computing *Chem. Mater.* **23** 3854–62
[30] Wang L, Maxisch T and Ceder G 2006 Oxidation energies of transition metal oxides within the GGA+U framework *Phys. Rev.* B **73** 195107
[31] Monkhorst H J and Pack J D 1976 Special points for Brillouin-zone integrations *Phys. Rev.* B **13** 5188–92

[32] Vanderbilt D 1990 Soft self-consistent pseudopotentials in a generalized eigenvalue formalism *Phys. Rev.* B **41** 7892–5
[33] Louie S G, Froyen S and Cohen M L 1982 Nonlinear ionic pseudopotentials in spin-density-functional calculations *Phys. Rev.* B **26** 1738–42
[34] Kresse G and Hafner J 1993 *Ab initio* molecular dynamics for liquid metals *Phys. Rev.* B **47** 558–61
[35] Kresse G and Furthmüller J 1996 Efficiency of *ab-initio* total energy calculations for metals and semiconductors using a plane-wave basis set *Comput. Mater. Sci.* **6** 15–50
[36] Kresse G and Furthmüller J 1996 Efficient iterative schemes for *ab initio* total-energy calculations using a plane-wave basis set *Phys. Rev.* B **54** 11169–86
[37] Blöchl P E 1994 Projector augmented-wave method *Phys. Rev.* B **50** 17953–79
[38] Kresse G and Joubert D 1999 From ultrasoft pseudopotentials to the projector augmented-wave method *Phys. Rev.* B **59** 1758–75
[39] Togo A and Tanaka I 2015 First principles phonon calculations in materials science *Scr. Mater.* **108** 1–5
[40] Gonze X and Lee C 1997 Dynamical matrices, born effective charges, dielectric permittivity tensors, and interatomic force constants from density-functional perturbation theory *Phys. Rev.* B **55** 10355–68
[41] Burke K and Ernzerhof M 1996 Generalized gradient approximation made simple *Phys. Rev. Lett.* **77** 3865
[42] Ceperley D M and Alder B J 1980 Ground state of the electron gas by a stochastic method *Phys. Rev. Lett.* **45** 566–9
[43] Sun J, Ruzsinszky A and Perdew J P 2015 Strongly constrained and appropriately normed semilocal density functional *Phys. Rev. Lett.* **115** 036402
[44] Heyd J, Scuseria G E and Ernzerhof M 2003 Hybrid functionals based on a screened Coulomb potential *J. Chem. Phys.* **118** 8207–15
[45] Krukau A V, Vydrov O A, Izmaylov A F and Scuseria G E 2006 Influence of the exchange screening parameter on the performance of screened hybrid functionals *J. Chem. Phys.* **125** 224106
[46] Buckeridge J Chemical potential limits analysis program (available at: https://github.com/jbuckeridge/cplap)
[47] Buckeridge J, Scanlon D O, Walsh A and Catlow C R A 2014 Automated procedure to determine the thermodynamic stability of a material and the range of chemical potentials necessary for its formation relative to competing phases and compounds *Comput. Phys. Commun.* **185** 330–8
[48] Henkelman G and Jónsson H 2000 Improved tangent estimate in the nudged elastic band method for finding minimum energy paths and saddle points *J. Chem. Phys.* **113** 9978–85
[49] Henkelman G, Uberuaga B P and Jónsson H 2000 A climbing image nudged elastic band method for finding saddle points and minimum energy paths *J. Chem. Phys.* **113** 9901–4
[50] Hjorth Larsen A *et al* 2017 The atomic simulation environment—a python library for working with atoms *J. Phys.: Condens. Matter* **29** 273002
[51] Ong S P, Richards W D, Jain A, Hautier G, Kocher M, Cholia S, Gunter D, Chevrier V L, Persson K A and Ceder G 2013 Python materials genomics (pymatgen): a robust, open-source python library for materials analysis *Comput. Mater. Sci.* **68** 314–9
[52] Ganose A M, Jackson A J and Scanlon D O 2018 Sumo: command-line tools for plotting and analysis of periodic **ab initio** calculations *J. Open Source Softw.* **3** 717
[53] Bradley C J and Cracknell A P 2010 *The Mathematical Theory of Symmetry in Solids: Representation Theory for Point Groups and Space Groups* (Oxford classic texts in the physical sciences) (Oxford: Oxford University Press)
[54] Huber S P *et al* 2020 AiiDA 1.0, a scalable computational infrastructure for automated reproducible workflows and data provenance *Sci. Data* **7** 300
[55] Uhrin M, Huber S P, Yu J, Marzari N and Pizzi G 2021 Workflows in AiiDA: engineering a high-throughput, event-based engine for robust and modular computational workflows *Comput. Mater. Sci.* **187** 110086
[56] Momma K and Izumi F 2008 VESTA: a three-dimensional visualization system for electronic and structural analysis *J. Appl. Crystallogr.* **41** 653–8
[57] Jain A *et al* 2013 The materials project: a materials genome approach to accelerating materials innovation *APL Mater.* **1** 011002
[58] Jain A, Hautier G, Moore C J, Ping Ong S, Fischer C C, Mueller T, Persson K A and Ceder G 2011 A high-throughput infrastructure for density functional theory calculations *Comput. Mater. Sci.* **50** 2295–310
[59] Kang K and Ceder G 2006 Factors that affect Li mobility in layered lithium transition metal oxides *Phys. Rev.* B **74** 094105
[60] Sicolo S, Mock M, Bianchini M and Albe K 2020 And yet it moves: $LiNiO_2$, a dynamic Jahn–Teller system *Chem. Mater.* **32** 10096–103
[61] Chen H, Freeman C L and Harding J H 2011 Charge disproportionation and Jahn-Teller distortion in $LiNiO_2$ and $NaNiO_2$: a density functional theory study *Phys. Rev.* B **84** 085108
[62] Das H, Urban A, Huang W and Ceder G 2017 First-principles simulation of the (Li–Ni–Vacancy)O phase diagram and its relevance for the surface phases in Ni-rich Li-ion cathode materials *Chem. Mater.* **29** 7840–51
[63] Rougier A, Delmas C and Chadwick A V 1995 Non-cooperative Jahn-Teller effect in $LiNiO_2$: an EXAFS study *Solid State Commun.* **94** 123–7
[64] Chen Z, Zou H, Zhu X, Zou J and Cao J 2011 First-principle investigation of Jahn–Teller distortion and topological analysis of chemical bonds in $LiNiO_2$ *J. Solid State Chem.* **184** 1784–90
[65] Molenda J, Wilk P and Marzec J 2002 Structural electrical and electrochemical properties of $LiNiO_2$ *Solid State Ion.* **146** 73–79
[66] Momeni M, Yousefi Mashhour H and Kalantarian M M 2019 New approaches to consider electrical properties, band gaps and rate capability of same-structured cathode materials using density of states diagrams: layered oxides as a case study *J. Alloys Compd.* **787** 738–43
[67] Gummow R, Thackeray M, David W and Hull S 1992 Structure and electrochemistry of lithium cobalt oxide synthesised at 400 °C *Mater. Res. Bull.* **27** 327–37
[68] Oishi M, Yamanaka K, Watanabe I, Shimoda K, Matsunaga T, Arai H, Ukyo Y, Uchimoto Y, Ogumi Z and Ohta T 2016 Direct observation of reversible oxygen anion redox reaction in Li-rich manganese oxide, Li_2MnO_3, studied by soft x-ray absorption spectroscopy *J. Mater. Chem.* A **4** 9293–302
[69] Kang K, Chen C-H, Hwang B J and Ceder G 2004 Synthesis electrochemical properties, and phase stability of Li_2NiO_2 with the *immm* structure *Chem. Mater.* **16** 2685–90
[70] Dahn J R, von Sacken U and Michal C A 1990 Structure and electrochemistry of $Li_{1\pm y}NiO_2$ and a new Li_2NiO_2 phase with the $Ni(OH)_2$ structure *Solid State Ion.* **44** 87–97
[71] Davidson I J, Greedan J E, Von Sacken U, Michal C A and McKinnon W R 1993 Short range and long range magnetic order in 1*T*-Li_2NiO_2 *J. Solid State Chem.* **105** 410–6
[72] Lin L, Qin K, Zhang Q, Gu L, Suo L, Hu Y, Li H, Huang X and Chen L 2021 Li-rich $Li_2[Ni_{0.8}Co_{0.1}Mn_{0.1}]O_2$ for anode-free lithium metal batteries *Angew. Chem., Int. Ed.* **60** 8289–96

[73] Cohen A J, Mori-Sánchez P and Yang W 2008 Insights into current limitations of density functional theory *Science* **321** 792–4
[74] Hautier G, Ong S P, Jain A, Moore C J and Ceder G 2012 Accuracy of density functional theory in predicting formation energies of ternary oxides from binary oxides and its implication on phase stability *Phys. Rev.* B **85** 155208
[75] Skelton J M, Burton L A, Oba F and Walsh A 2017 Chemical and lattice stability of the tin sulfides *J. Phys. Chem.* C **121** 6446–54
[76] Sun W, Dacek S T, Ong S P, Hautier G, Jain A, Richards W D, Gamst A C, Persson K A and Ceder G 2016 The thermodynamic scale of inorganic crystalline metastability *Sci. Adv.* **2** e1600225
[77] Xu J, Hu E, Nordlund D, Mehta A, Ehrlich S N, Yang X-Q and Tong W 2016 Understanding the degradation mechanism of lithium nickel oxide cathodes for Li-ion batteries *ACS Appl. Mater. Interfaces* **8** 31677–83
[78] Li H, Zhang N, Li J and Dahn J R 2018 Updating the structure and electrochemistry of Li_xNiO_2 for $0 \leqslant x \leqslant 1$ *J. Electrochem. Soc.* **165** A2985–93
[79] Wang Y, Liu J, Chen T, Lin W and Zheng J 2022 Factors that affect volume change during electrochemical cycling in cathode materials for lithium ion batteries *Phys. Chem. Chem. Phys.* **24** 2167–75
[80] Xiong F, Yan H, Chen Y, Xu B, Le J and Ouyang C 2012 The atomic and electronic structure changes upon delithiation of $LiCoO_2$: from first principles calculations *Int. J. Electrochem. Sci.* **7** 9390–400
[81] Hoang K and Johannes M D 2018 Defect physics in complex energy materials *J. Phys.: Condens. Matter* **30** 293001
[82] Maxisch T, Zhou F and Ceder G 2006 *Ab initio* study of the migration of small polarons in olivine Li_xFePO_4 and their association with lithium ions and vacancies *Phys. Rev.* B **73** 104301
[83] Kim U-H *et al* 2018 Pushing the limit of layered transition metal oxide cathodes for high-energy density rechargeable Li ion batteries *Energy Environ. Sci.* **11** 1271–9
[84] Pouillerie C, Croguennec L, Biensan P, Willmann P and Delmas C 2000 Synthesis and characterization of new $LiNi_{1-y}Mg_yO_2$ positive electrode materials for lithium-ion batteries *J. Electrochem. Soc.* **147** 2061
[85] Kang K, Morgan D and Ceder G 2009 First principles study of Li diffusion in I-Li_2NiO_2 structure *Phys. Rev.* B **79** 014305
[86] Ma X, Kang B and Ceder G 2010 High rate micron-sized ordered $LiNi_{0.5}Mn_{1.5}O_4$ *J. Electrochem. Soc.* **157** A925
[87] Van der Ven A and Ceder G 2001 Lithium diffusion mechanisms in layered intercalation compounds *J. Power Sources* **97–98** 529–31
[88] Freysoldt C, Grabowski B, Hickel T, Neugebauer J, Kresse G, Janotti A and Van de Walle C G 2014 First-principles calculations for point defects in solids *Rev. Mod. Phys.* **86** 253–305
[89] Chase M W 1998 *NIST-JANAF Thermochemical Tables* 4th edn (Washington, DC; New York: American Chemical Society; American Institute of Physics) (https://doi.org/10.18434/T42S31)
[90] Bartel C J, Millican S L, Deml A M, Rumptz J R, Tumas W, Weimer A W, Lany S, Stevanović V, Musgrave C B and Holder A M 2018 Physical descriptor for the Gibbs energy of inorganic crystalline solids and temperature-dependent materials chemistry *Nat. Commun.* **9** 4168
[91] Timrov I, Aquilante F, Cococcioni M and Marzari N 2022 Accurate electronic properties and intercalation voltages of olivine-type Li-ion cathode materials from extended Hubbard functionals *PRX Energy* **1** 033003
[92] Shishkin M and Sato H 2016 Self-consistent parametrization of DFT + U framework using linear response approach: application to evaluation of redox potentials of battery cathodes *Phys. Rev.* B **93** 085135
[93] Timrov I, Marzari N and Cococcioni M 2021 Self-consistent Hubbard parameters from density-functional perturbation theory in the ultrasoft and projector-augmented wave formulations *Phys. Rev.* B **103** 045141
[94] Xu Z, Joshi Y V, Raman S and Kitchin J R 2015 Accurate electronic and chemical properties of 3d transition metal oxides using a calculated linear response U and a DFT + U(V) method *J. Chem. Phys.* **142** 144701
[95] Cen J, Zhu B and Scanlon D 2023 Dataset for: Exploring Battery Cathode Materials in the Li-Ni-O Phase Diagrams using Structure Prediction Zenodo (https://doi.org/10.5281/zenodo.8022111)